Supplementary Materials for "Signatures of quantum chaos in phonon-polariton billiards"

CONTENTS

1. EXPERIMENTAL METHODS

To prepare the samples, we exfoliate isotopically enriched hBN (^{10}B) crystals onto silicon substrates with a 285 nm SiO_2 layer. The flake thickness and surface cleanliness are prescreened by optical microscopy based on optical contrast, and subsequently verified by atomic force microscopy (AFM). The selected hBN flake is then transferred onto a silicon chip patterned with gold alignment markers using a PDMS (polydimethylsiloxane) stamp coated with a PPC (polypropylene carbonate) film. We use electron beam lithography to define the desired cavity geometry, followed by reactive ion etching with SF_6 to remove excess material. After fabrication, the sample is annealed at 400 °C in forming gas (5% H_2 and 95% N_2) for 10 minutes to remove residual PMMA and PPC.

Nano-imaging experiments were carried out at room temperature under ambient conditions using a commercial scattering-type scanning near-field optical microscope (s-SNOM) equipped with an FTIR module (Neaspec). Metallic AFM tips (NanoWorld) with an apex diameter of approximately 20 nm were operated in tapping mode, oscillating vertically with an amplitude of 60–120 nm. The AFM tips both locally launch polaritonic modes and outcouple the electromagnetic waves carrying information about the polariton fields. For single-color imaging experiments, tunable continuous-wave mid-infrared quantum cascade lasers (Daylight Solutions) were used. The single-color near-field imaging was performed using a pseudo-heterodyne interferometric scheme, in which the reference mirror was modulated at a frequency of several hundred hertz in addition to the tip oscillation frequency ($\sim$75 kHz). For hyperspectral imaging experiments, broadband mid-infrared pulses from difference frequency generation (DFG) utilized outputs of a dual channel optical parametric amplifier (OPA, Orpheus Twins). The amplifier was pumped by a 20 W, 1030 nm Yb:KGW laser (Pharos, Light Conversion) operating at 755 kHz. The idler was fixed at 1500 nm and the signal tuned to 1940 nm to produce broadband mid-infrared radiation. A piezo-driven stage was used to translate the reference mirror, allowing frequency-resolved measurements via a Michelson interferometer. The broadband near-field signals were detected using a self-homodyne interferometric scheme.

2. THEORETICAL MODEL

A. Phonon-polariton dispersion

Figures 1e-g of the main text were generated as follows. The in-plane momenta $k_l(\omega)$ of $l \neq 0$ phonon-polariton modes were computed from

$$k_l(\omega) = i\frac{\sqrt{\varepsilon^z}}{\sqrt{\varepsilon^\perp}}\, k_{z,l}\,, \qquad k_{z,l} = \frac{\pi}{d}\,(l + \delta_z)\,, \tag{S1}$$

where the dimensionless function $\delta_z = \delta_z(\omega)$ is related to the phase shift of internal reflections off the top and bottom surfaces of the hBN. We approximated this function by [1]

$$\delta_z = \frac{1}{\pi}\,\arctan\left(i\frac{\varepsilon_0}{\varepsilon}\right) + \frac{1}{\pi}\,\arctan\left(i\frac{\varepsilon_2}{\varepsilon}\right), \qquad \varepsilon \equiv \left(\varepsilon^\perp \varepsilon^z\right)^{1/2}, \tag{S2}$$

where $\varepsilon_2(\omega)$ and $\varepsilon_0(\omega)$ are the permittivities of, respectively, the substrate (SiO_2) and the superstrate (air) of the hBN layer. Equation (S2) is obtained assuming k_l is large, which normally requires k_l only to be larger than the free-photon momentum $k_{\text{ph}} = 2\pi\omega$. In the present case, however, there is another large parameter $|\varepsilon| \gg \varepsilon_0, \varepsilon_2$ in the problem at frequencies near the bottom of the Reststrahlen band (RB). As a result, Eq. (S2) becomes inaccurate already fairly far away from the light cone. For $l \neq 0$ modes this is not very important because δ_z is a small correction to $l + \delta_z$. For the $l = 0$ mode, a more refined approximation is needed, which is as follows:

$$\frac{\varepsilon_0 k_{\text{ph}}}{\sqrt{\varepsilon_0 k_{\text{ph}}^2 - k_0^2}} + \frac{\varepsilon_2 k_{\text{ph}}}{\sqrt{\varepsilon_2 k_{\text{ph}}^2 - k_0^2}} = -\frac{4\pi\sigma}{c}\,, \tag{S3}$$

where

$$\frac{4\pi\sigma}{c} \equiv -i\varepsilon^{\perp}(\omega) k_{\text{ph}} d\,. \tag{S4}$$

The derivation of this equation and the meaning of parameter σ are discussed in Sec. 2 B. To calculate k_0 as a function of ω, we transformed Eq. (S3) to a fourth-degree algebraic equation and found its physically relevant root numerically. (This is the root with positive real and imaginary parts.) If $k_0 \gg k_{\text{ph}}$, the solution admits the analytical form

$$k_0(\omega) \simeq -\frac{\varepsilon_0(\omega) + \varepsilon_2(\omega)}{\varepsilon^{\perp}(\omega)}\,\frac{1}{d}\,, \tag{S5}$$

which agrees with Eqs. (S1) and (S2) in the limit $\varepsilon \gg \varepsilon_0, \varepsilon_2$. The condition $\operatorname{Re} \varepsilon^{\perp}(\omega) < 0$ ensures that the requirement $\operatorname{Re} k_0 > 0$ mentioned above is met; otherwise, the hyperbolicity of hBN plays no role since the out-of-plane permittivity $\varepsilon^{z}(\omega)$ no longer enters the equations. Physically, this is because the z-component of the electric field inside the hBN layer is very small in this regime.

B. 2D wave equation for polaritons

In this subsection we derive Eq. (S3) and explain how it leads to Eq. (1) of the main text. Equation (S3) is written in this specific form to emphasize that it is identical to the equation for the dispersion of plasmon-polaritons in a 2D film with conductivity σ. By definition, the conductivity is the coefficient of proportionality between in-plane electric field $\mathbf{E}_{\perp}$ and the 2D current density $\mathbf{J} = \sigma \mathbf{E}_{\perp}$. Let us show that Eq. (S4) reproduces this relation correctly for a highly polarizable dielectic layer occupying a slab $-d/2 < z < d/2$ of small thickness d. Indeed, if $d \ll 1/k_0$, then the electric field $\mathbf{E}_{\perp}$ of the polariton and the polarization

$$\mathbf{P}_{\perp} = \frac{\varepsilon^{\perp} - 1}{4\pi}\,\mathbf{E}_{\perp}$$

it induces inside the layer are nearly uniform. Therefore,

$$\mathbf{J}(x,y,z) = \int\limits_{-d/2}^{d/2} \mathbf{j}(x,y,z)dz = -i\omega \int\limits_{-d/2}^{d/2} \mathbf{P}_\perp(x,y,z)dz \simeq -i\omega d\,\mathbf{P}_\perp(x,y,0)\,.$$

Assuming $\varepsilon^\perp$ is large, so that $\varepsilon^\perp - 1 \simeq \varepsilon^\perp$, we obtain Eq. (S4).

Next, to derive Eq. (S3), we consider a single Fourier harmonic, $\mathbf{E}_\perp = \tilde{\mathbf{E}}_\perp(\mathbf{k}_\perp, z)e^{ik_x x + ik_y y}$. Outside the layer, the amplitude $\tilde{\mathbf{E}}_\perp(\mathbf{k}_\perp, z)$ behaves as

$$\tilde{\mathbf{E}}_\perp(\mathbf{k}_\perp, z) = \tilde{\mathbf{E}}_\perp(\mathbf{k}_\perp, 0)\exp\left(i\sqrt{\varepsilon_j k_{\mathrm{ph}}^2 - k^2}\,|z|\right), \tag{S6}$$

where $j = 0$ for $z > 0$ and $j = 2$ for $z < 0$. For any nonvanishing dissipation, $\operatorname{Im}\varepsilon_j > 0$, the square roots have positive imaginary parts for all real $k = \sqrt{k_x^2 + k_y^2}$ and the standard choice of the branch cut, so that the electric field decays exponentially on both sides of the layer. The modes we are interested in are transverse magnetic (TM), in the sense that the in-plane electric field is longitudinal, $\mathbf{E}_\perp \parallel \mathbf{k}_\perp$, while the magnetic field is purely transverse, $\mathbf{H} \parallel [\hat{\mathbf{z}} \times \mathbf{k}_\perp]$. For this case, it is easy to show that the amplitude of the magnetic field is given by

$$\tilde{\mathbf{H}}_\perp(\mathbf{k}_\perp, z) = \operatorname{sgn} z\,\frac{\varepsilon_j k_{\mathrm{ph}}}{\sqrt{\varepsilon_j k_{\mathrm{ph}}^2 - k^2}}\,\hat{\mathbf{z}} \times \tilde{\mathbf{E}}_\perp(\mathbf{k}_\perp, z), \qquad \operatorname{sgn} z = \frac{z}{|z|}\,. \tag{S7}$$

Using the boundary condition (BC) on the tangential component of $\mathbf{H}$,

$$\left[\mathbf{H}_\perp\left(x, y, \frac{d}{2}\right) - \mathbf{H}_\perp\left(x, y, -\frac{d}{2}\right)\right] \times \hat{\mathbf{z}} = -\frac{4\pi}{c}\,\mathbf{J}(x,y) = -\frac{4\pi\sigma}{c}\,\mathbf{E}_\perp(x,y,0)\,, \tag{S8}$$

we see that a nontrivial solution exists only when Eq. (S3) is satisfied.

In general, the electric field created by a polarized dielectric layer can be represented by a Fourier integral

$$\mathbf{E}_\perp(x,y) = -\nabla_\perp\psi(x,y) = \int \frac{dk_x dk_y}{(2\pi)^2}\,\tilde{\mathbf{E}}_\perp(\mathbf{k}_\perp)e^{ik_x x + ik_y y}\,, \qquad \tilde{\mathbf{E}}_\perp(\mathbf{k}_\perp) = -i\mathbf{k}_\perp\tilde{\psi}(\mathbf{k}_\perp), \tag{S9}$$

where we dropped the argument $z = 0$ for simplicity and enforced the constraint that the field is TM by introducing a scalar potential $\psi(x,y)$.

According to the continuity equation $\nabla_\perp \cdot \mathbf{J}(x,y) = iw\rho(x,y)$ where $\rho(x,y)$ is the charge density per unit area and $w = k_{\mathrm{ph}}c$ is the frequency (not to be confused with the inverse photon wavelength $\omega = k_{\mathrm{ph}}/2\pi$). Taking the divergence of both sides of Eq. (S8), we obtain

$$\rho(x,y) = \frac{i}{w}\,\nabla_\perp \cdot [\sigma(x,y)\nabla_\perp\psi(x,y)] = \int \frac{dk_x dk_y}{(2\pi)^2}\frac{\tilde{\psi}(\mathbf{k}_\perp)}{K(k)}\,e^{ik_x x + ik_y y}, \tag{S10}$$

$$\frac{1}{K(k)} \equiv i\,\frac{k^2}{4\pi}\left(\frac{\varepsilon_0}{\sqrt{\varepsilon_0 k_{\mathrm{ph}}^2 - k^2}} + \frac{\varepsilon_2}{\sqrt{\varepsilon_2 k_{\mathrm{ph}}^2 - k^2}}\right). \tag{S11}$$

After the inverse Fourier transform, the first equation can also be written

$$\psi(x,y) = \int \frac{dk_x dk_y}{(2\pi)^2} K(k)\tilde{\rho}(\mathbf{k}_\perp)\, e^{ik_x x + ik_y y}, \tag{S12}$$

which clarifies the physical meaning of $K(k)$ as the 2D Coulomb interaction kernel. In the quasistatic limit $k \gg k_{\rm ph}$ it approaches $K(k) = 2\pi/(\kappa k)$ with $\kappa = (\varepsilon_0 + \varepsilon_2)/2$. Note that $\sigma = \sigma(x,y)$ in Eq. (S10) is allowed to be position-dependent in general, which makes Eq. (S10) applicable to not just an infinite slab but also any finite-size plate. In the latter case function $\sigma(x,y)$ has a step-like discontinuity. It takes a constant value $\sigma \neq 0$ inside the plate and is zero outside. Another generalization we can make is to replace $\psi(x,y)$ with

$$\psi_{\rm tot}(x,y) = \psi(x,y) + \psi_{\rm ext}(x,y) \tag{S13}$$

on the left-hand side of Eq. (S10) in order to include an external potential $\psi_{\rm ext}(x,y)$ due to near-field sources outside the dielectric layer such as the scanned probe. The equations we derived are identical to those for plasmon-polaritons. Their quasistatic (plasmonic) limit is particularly well-known.

The integro-diffential Eq. (S10) is difficult to tackle with standard numerical solvers. Since we are mainly interested in the wave patterns formed by polaritons with momentum $k \approx k_0$, we simplify the problem by expanding $K^{-1}(k)$ near k_0:

$$\frac{1}{K(k)} \approx \frac{1}{K(k_0)} + \left[\frac{1}{2k}\frac{d}{dk}\frac{1}{K(k)}\right]_{k=k_0} (k^2 - k_0^2)\,, \qquad \frac{1}{K(k_0)} = \frac{\sigma}{iw}\, k_0^2\,. \tag{S14}$$

The term $k^2 - k_0^2$ in the Fourier integral is equivalent to $-\Delta - k_0^2$ in the real space, where $\Delta \equiv \nabla_\perp^2$ is the 2D Laplacian. With this subsitution, we arrive at the scalar 2D Helmholtz equation, Eq. (1) of the main text:

$$\left(\Delta + k_0^2\right)\psi(x,y) = F(x,y)\,, \qquad (x,y) \in \Omega\,, \tag{S15}$$

where Ω is the domain where $\sigma \neq 0$. The source term on the right-hand side is given by

$$F(x,y) = -\left[1 + \frac{k_0}{2}\frac{K'(k_0)}{K(k_0)}\right]^{-1} \Delta\psi_{\rm ext}(x,y) \simeq -2\Delta\psi_{\rm ext}(x,y), \tag{S16}$$

with the last equation being valid in the quasistatic limit. Within the same accuracy, we could replace the right-hand side by $2k_0^2\psi_{\rm ext}$ or better, by $(-\Delta + k_0^2)\psi_{\rm ext}$. In the latter case the high-momentum harmonics of the solution would be also reproduced correctly: $\tilde{\psi}(\mathbf{k}_\perp) \simeq -\tilde{\psi}_{\rm ext}(\mathbf{k}_\perp)$ at $k \gg k_0$ (the perfect screening condition).

C. Edge reflections and boundary conditions

Equation (S15) needs to be supplemented with the BC at the edges. In our simulations, we adopt the following Robin BC:

$$\partial_n \psi + \mathcal{R}\psi = 0\,, \qquad (x, y) \in \partial\Omega\,, \tag{S17}$$

where ∂_n is the outward normal derivative and $\mathcal{R}$ is a constant specified below.

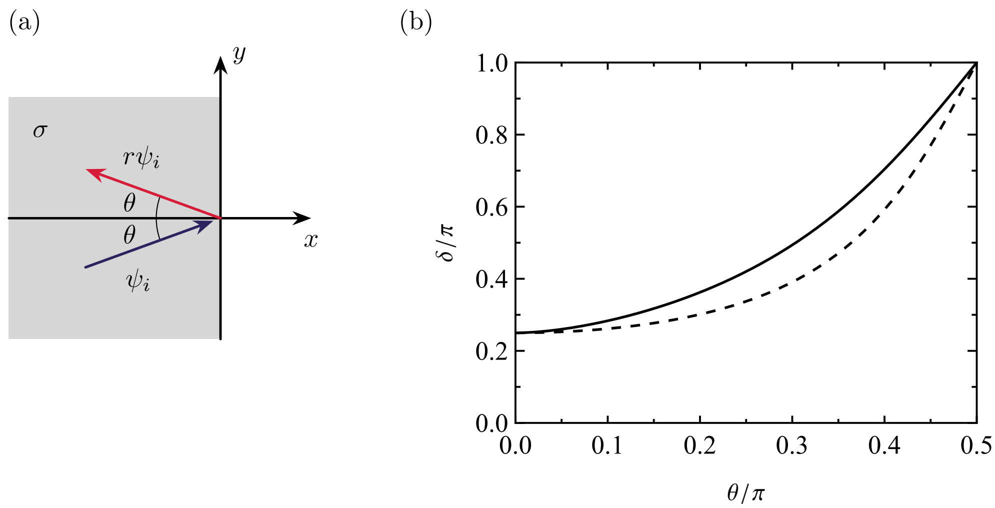

FIG. S1. (a) Geometry of the edge scattering problem. (b) The reflection phase shift δ as a function of the angle of incidence θ. The solid and dashed lines represent, respectively, Eqs. (S22) and (S24).

Let us explain the genesis of Eq. (S17). Consider a scattering problem where a polariton is incident on an ideal straight edge, see Fig. S1(a). In general, this polariton can be reflected back into the interior of the sample or scattered into the free-space as a photon. If the polariton is highly confined, $k_0 \gg k_{\mathrm{ph}}$, the reflection is the dominant process. Let us choose the y-axis along the edge, so that Ω is the half-plane $x < 0$. Suppose the incident wave has an amplitude ψ_i and a transverse momentum k_y, then the total potential $\psi(x, y)$ is

$$\psi(x, y) \simeq \psi_i e^{ik_y y}\left(e^{ik_x x} + r e^{-ik_x x}\right), \qquad x \to -\infty\,, \tag{S18}$$

where k_x is such that $k_0^2 = k_x^2 + k_y^2$. The reflection coefficient $r = e^{i\delta}$ in Eq. (S18) is a complex number with a unit absolute value and argument $\delta = \delta(\theta)$, which is some function of the angle of incidence $\theta = \arcsin(k_y/k_0)$. Crucially, even though Eq. (S18) applies only in the asymptotic region $|x| \gg k_x^{-1}$, if we use Eq. (S15) in the entire half-plane, then the following BC imposed at $x = 0$ reproduces this asymptotic behavior correctly:

$$\partial_x \psi + k_0 f(\theta)\psi = 0\,, \qquad f(\theta) \equiv -\tan\frac{\delta(\theta)}{2}\cos\theta\,. \tag{S19}$$

In principle, it is possible to implement such a BC for an arbitrary $\delta(\theta)$ by replacing θ with the operator

$$\theta = \arcsin\left(\frac{k_y}{k_0}\right) \to \arcsin\left(-\frac{i}{k_0}\partial_y\right). \tag{S20}$$

In practice, doing so would be too complicated unless we neglect the angle dependence of function $f(\theta)$ and replace it by $f(0)$. This gives

$$\partial_x\psi + \mathcal{R}\psi = 0\,, \qquad \mathcal{R} \equiv -k_0 \tan\frac{\delta(0)}{2}\,. \tag{S21}$$

In a finite domain, we change ∂_x to ∂_n and arrive at Eq. (S17).

To fix the value of the Robin constant $\mathcal{R}$ we need to know $\delta(0)$. Notice that $\delta(0) = 0$ and $\delta(0) = \pi$ would yield the usual Neumann and the Dirichlet BC, respectively. To find the correct $\delta(0)$ we use the mapping to plasmon-polaritons: since the $l = 0$ phonon-polaritons obey the same equation as 2D plasmon-polaritons, their reflection phase shift is also the same. Furthermore, if the polariton confinement is strong, $k_0 \gg k_{\text{ph}}$, this phase shift can be approximated by that for 2D plasmons, which has been well studied. The most recent calculation we are aware of is Ref. [2], where references to previous work can also be found. In a more general formulation, the scattering occurs at a junction of two semi-infinite planes with conductivities σ_L and σ_R. The reflection off the physical edge corresponds to $\sigma_L = \sigma$ and $\sigma_R = 0$. When analyzed further, the equations [2] for r can be used to represent $\delta(\theta)$ in a closed form:

$$\delta(\theta) = 2\arctan\left\{\tan\theta\tanh\left[\frac{2}{\pi}\,\mathrm{Im}\,\chi_2\left(e^{i\theta}\right)\right]\right\} + \frac{2}{\pi}\,\chi_2(\cos\theta)\,. \tag{S22}$$

Here $\chi_2(z)$ is the Legendre chi function of order 2, which is the odd part of the dilogarithm function $\mathrm{Li}_2(z)$:

$$\chi_2(z) \equiv \frac{1}{2}\left[\mathrm{Li}_2(z) - \mathrm{Li}_2(-z)\right] = \int_0^z \frac{dt}{2t}\,\ln\left(\frac{1+t}{1-t}\right). \tag{S23}$$

In particular, $\chi_2(0) = \pi^2/8$ and so $\delta(0) = \pi/4$ [3]. The plot of $\delta(\theta)$ computed from Eq. (S22) is shown in Fig. S1(b) together with the approximation

$$\delta(\theta) = 2\arctan\left(\tan\frac{\delta(0)}{2}\,\sec\theta\right), \tag{S24}$$

which is equivalent to the Robin BC (S21). As one can see, with $\delta(0)$ anchored to the exact result of $\pi/4$, this approximation is reasonably accurate in the entire range of θ.

D. Edge polaritons

One of the key experimental observations is the presence of the polariton edge modes. These effectively one-dimensional modes are localized at the edge and decay exponentially into the interior of the sample. The standard way to compute their dispersion is to look for the poles of the edge reflection coefficient r as a function of real $k_y = k_0 \sin\theta$. For the edge modes, k_y must exceed k_0 to be outside the bulk continuum. Thus, θ and $k_x = i\sqrt{k_y^2 - k_0^2}$ must be complex numbers. If we use the exact Eq. (S22), the solution is known to be [4]

$$\frac{k_y}{k_0} = 1.217\,. \tag{S25}$$

As mentioned earlier, the reflection coefficient describes the asymptotic behavior of the mode. The exponential decay $\psi(x,y) \propto e^{-|k_x x|}$ is established after $|x|$ exceeds the width $\sim 1/|k_x|$ of the transient region.

For the Robin BC (S17), which is equivalent to the approximate Eq. (S24), k_y is a bit smaller,

$$\frac{k_y}{k_0} = \sec\frac{\delta(0)}{2} = \sec\frac{\pi}{8} = 1.082\,, \tag{S26}$$

and the mode profile is pure exponential, $\psi(x,y) \propto e^{ik_x x}$, at all $x \leq 0$. Notice that having $0 < \delta(0) < \pi$ intermediate between the Dirichlet and Neumann limits is necessary for the existence of the edge modes.

In a finite-size billiard, the spectrum of the edge modes becomes quantized. For example, if we assume that that the edge modes experience full reflections at the end points of a straight edge of length L, the allowed momenta k_y obey the equation

$$k_y L = 2\pi n - \delta_1 - \delta_2\,, \tag{S27}$$

where δ_1, δ_2 are the reflection phase shifts and n is an integer.

E. Simulation framework

In the preceding sections we established that Eq. (S15) with the BC Eq. (S17) provide a reasonable approximation for modeling the propagation of $l = 0$ phonon-polaritons inside hBN billiards of large enough size $L \gg k_0^{-1}$. The solution of this boundary-value problem can be written as

$$\psi(x,y) = \int G(x,y;x_0,y_0) F(x_0,y_0) dx_0 dy_0\,, \tag{S28}$$

where $G(x, y; x_0, y_0)$ is the Green's function (GF). This function is given by the series

$$G(x, y; x_0, y_0) = \sum_{n=1}^{\infty} \frac{\psi_n(x, y)\psi_n^*(x_0, y_0)}{k_0^2(\omega) - E_n}\,, \tag{S29}$$

where $\psi_n(x, y)$ are the eigenfunctions labeled in the increasing order of their eigenvalues E_n. The only difference from the standard Dirichlet or Neumann GF is that when solving the eigenvalue problem, we use $k_0 = \sqrt{E_n}$, i.e., our Robin parameter $\mathcal{R} = \mathcal{R}(E_n)$ is eigenvalue-dependent. This nonlinear eigenvalue problem is solved by iterations.

Let us now summarize general principles for modeling the s-SNOM imaging. We will use Dirac's bra-ket notation to denote functions and bold symbols to denote operators acting on them. Thus, Eq. (S28) becomes

$$|\boldsymbol{\psi}\rangle = \mathbf{G}|\mathbf{F}\rangle = -2k_0^2\mathbf{G}|\boldsymbol{\psi}_{ext}\rangle\,. \tag{S30}$$

If the geometry of the tip of the near-field probe is described by $|\mathbf{r}_t\rangle$ and its charge density distribution by $|\boldsymbol{\rho}_t\rangle$, then the s-SNOM signal S is proportional to the (oscillating with frequency w) dipole moment of the tip

$$S \propto \langle\mathbf{r}_t|\boldsymbol{\rho}_t\rangle\,. \tag{S31}$$

Suppose the tip is perfectly conducting, then the potential on its surface must vanish:

$$|\boldsymbol{\psi}_t\rangle = \mathbf{K}_{tt}|\boldsymbol{\rho}_t\rangle + \mathbf{K}_{ts}|\boldsymbol{\rho}\rangle - E_0|\mathbf{r}_t\rangle = 0\,, \tag{S32}$$

where $\mathbf{K}_{tt}$ and $\mathbf{K}_{ts}$ are the operators representing the tip-tip and tip-sample interactions. Parameter E_0 is the approximately uniform electric field illuminating the tip, which consists from the incident field from the laser plus the far-field component of this field reflected off the sample. We also have $|\boldsymbol{\rho}\rangle = \mathbf{K}^{-1}|\boldsymbol{\psi}\rangle$ and

$$|\boldsymbol{\psi}_{ext}\rangle = \mathbf{K}_{st}|\boldsymbol{\rho}_t\rangle = \mathbf{K}_{ts}^{\dagger}|\boldsymbol{\rho}_t\rangle\,, \tag{S33}$$

by the reciprocity theorem. Combining all these equations, and absorbing E_0 and the overall constant into the kernels, we find

$$S = \langle\mathbf{r}_t|\left(\mathbf{K}_{tt} - 2k_0^2\,\mathbf{K}_{ts}\mathbf{K}^{-1}\mathbf{G}\mathbf{K}_{ts}^{\dagger}\right)^{-1}|\mathbf{r}_t\rangle\,. \tag{S34}$$

It may be convenient to switch from the description of the tip geometry in Cartesian coordinates to some other orthogonal basis, $|\mathbf{e}\rangle = \mathbf{U}\,|\mathbf{r}_t\rangle$, in which case the tip-tip interaction operator changes to $\boldsymbol{\Lambda} = \mathbf{U}\mathbf{K}_{tt}\mathbf{U}^{\dagger}$. The formula for S becomes

$$S = \langle\mathbf{e}|\left(\boldsymbol{\Lambda} - \mathbf{HGH}\right)^{-1}|\mathbf{e}\rangle\,, \tag{S35}$$

where $\mathbf{H}$ can be expressed in terms of $\mathbf{\Lambda}$ and other operators introduced above. Note that it depends on the tip-sample distance z_{tip}.

The above expression is formally exact but laborious to implement, so it is usually approximated in some way. Here, we treat the response of the sample as a perturbation and expand S to the first order:

$$S \approx \langle \mathbf{e}|\mathbf{\Lambda}^{-1}|\mathbf{e}\rangle + \langle \mathbf{e}_1|\mathbf{HGH}|\mathbf{e}_1\rangle \,, \qquad |\mathbf{e}_1\rangle = \mathbf{\Lambda}^{-1}|\mathbf{e}\rangle \,. \tag{S36}$$

In the coordinate representation, this equation entails, roughly,

$$S(x_{\text{tip}}, y_{\text{tip}}) = S_0 + \sum_{n=1}^{\infty} \frac{|h * \psi_n|^2}{k_0^2(\omega) - E_n} \,, \qquad h * \psi_n = \int h(x - x_{\text{tip}}, y - y_{\text{tip}})\psi_n(x, y) dx dy \,, \tag{S37}$$

where the kernel $h(x, y)$ is a certain function that decays to zero over a distance of the order of $r_{\max} = \max(z_{\text{tip}}, a)$, where a is the tip radius. The first term S_0 is the signal measured far away from the sample. It is in fact the largest term but it is removed by demodulating S with respect to $z_{\text{tip}} = z_{\text{tip}}(t)$. We drop this term and simplify the above expression further simply by truncating the series:

$$S(x, y) = \sum_{n=1}^{N} \frac{|\psi_n(x, y)|^2}{k_0^2(\omega) - E_n} \,, \tag{S38}$$

where the upper cutoff N is such that $E_N r_{\max}^2 \sim 1$. Within the presented framework, the dependence of the observed images on the tip tapping amplitude comes from choosing different N. In the plots of our experimental data we show the absolute value $|S(x, y)|$ of the complex number $S(x, y)$.

The right-hand side of Eq. (S38) is essentially the diagonal part of the GF, Eq. (S29). In our modeling, we use a slightly different expression,

$$S(x, y) = \sum_{n=1}^{N} \frac{|\psi_n(x, y)|^2}{(\omega + i\gamma_n)^2 - \omega_n^2} \,, \tag{S39}$$

which emphasizes the similarity with the standard formulas for GFs of phononic systems. It is expected to produce similar results because the difference $|S(x, y)| - \langle |S(x, y)| \rangle$, i.e., the near-field contrast, is dominated by the same eigenmodes in both Eqs. (S38) and (S39): the modes with $E_n \approx k_0^2(\omega)$. In our simulations, we computed $\psi_n(\mathbf{r})$ and E_n using the finite-element method [5] and retain the first $N = 200$ eigenmodes. We deduced the eigenfrequencies ω_n from E_n's by solving $E_n = \operatorname{Re} k_0^2(\omega_n)$, where $k_0(\omega)$ is the phonon-polariton dispersion discussed in Sec. 2 A. We took the polariton damping rate in Eq. (S39) to be $\gamma_n = \omega_n/(2Q)$, where Q is a constant quality factor.

Our numerical results obtained within this approach are in a good qualitative agreement with the experimental results, as can be seen in Fig. 2 and 3 of the main text. In particular, we recover essential spectral and spatial polaritonic features of the Sinai billiard.

F. Berry's circles

A given eigenfunction can always be decomposed into Fourier harmonics

$$\psi_n(x,y) = \int \frac{dk_x dk_y}{(2\pi)^2} \tilde{\psi}_n(\mathbf{k}_\perp)\, e^{ik_x x + ik_y y}. \tag{S40}$$

According to Berry's random wave conjecture, for classically chaotic systems, the Fourier amplitudes $\tilde{\psi}_n(\mathbf{k}_\perp)$ of dominant harmonics are isotropically distributed on some circle in the momentum space, i.e., these eigenfunctions are random superpositions of plane waves with fixed wavenumber and uniformly distributed propagation directions [6]. A more precise statement is that $\tilde{\psi}_n(\mathbf{k}_\perp)$ are complex Gaussian random variables with zero mean and correlation function

$$\left\langle \tilde{\psi}_n(\mathbf{q}_1)\tilde{\psi}_n(\mathbf{q}_2) \right\rangle = C(\mathbf{q}_1)\delta_{\mathbf{q}_1,-\mathbf{q}_2}\,, \qquad C(\mathbf{q}) = \frac{2\pi}{\sqrt{E_n}}\delta\left(|\mathbf{q}| - \sqrt{E_n}\right). \tag{S41}$$

For time-reversal invariant systems (GOE), we can choose $\psi_n(x,y)$ to be real, in which case $\tilde{\psi}_n(-\mathbf{q}) = \tilde{\psi}_n^*(\mathbf{q})$. The formula for $C(\mathbf{q})$ is certainly approximate. Instead of the ideal δ-function, it should be a function with some finite spread around the circle $k = \sqrt{E_n}$. However, Berry's conjecture is silent on what this spread is.

Armed with this conjecture, let us examine what it implies for the Fourier transform of the squared $\psi_n(x,y)$:

$$\tilde{I}_n(\mathbf{k}_\perp) \equiv \int dxdy\, e^{-ik_x x - ik_y y}|\psi_n(x,y)|^2 = \frac{1}{|\Omega|}\sum_{\mathbf{q}} \tilde{\psi}_n(\mathbf{q})\tilde{\psi}_n(\mathbf{k}_\perp - \mathbf{q})\,, \tag{S42}$$

where $|\Omega|$ is the area of the domain Ω. It is easy to see that the mean of $\tilde{I}_n(\mathbf{k}_\perp)$ vanishes unless $\mathbf{k}_\perp = 0$:

$$\langle \tilde{I}_n(\mathbf{k}_\perp)\rangle = \int \frac{dq_x dq_y}{(2\pi)^2}\, C(\mathbf{q})\delta_{\mathbf{k}_\perp,0} = \delta_{\mathbf{k}_\perp,0}\,. \tag{S43}$$

However, the mean of its squared absolute value is nonvanishing:

$$\begin{aligned}
\langle|\tilde{I}_n(\mathbf{k}_\perp)|^2\rangle &= \frac{1}{|\Omega|^2}\sum_{\mathbf{q}_1,\mathbf{q}_2}\left\langle\tilde{\psi}_n(\mathbf{q}_1)\tilde{\psi}_n(\mathbf{k}_\perp-\mathbf{q}_1)\tilde{\psi}_n(\mathbf{q}_2)\tilde{\psi}_n(\mathbf{k}_\perp-\mathbf{q}_2)\right\rangle \\
&= \frac{1}{|\Omega|^2}\sum_{\mathbf{q}_1,\mathbf{q}_2}\left\langle\tilde{\psi}_n(\mathbf{q}_1)\tilde{\psi}_n(\mathbf{k}_\perp-\mathbf{q}_1)\right\rangle\left\langle\tilde{\psi}_n(\mathbf{q}_2)\tilde{\psi}_n(\mathbf{k}_\perp-\mathbf{q}_2)\right\rangle \\
&+ \frac{1}{|\Omega|^2}\sum_{\mathbf{q}_1,\mathbf{q}_2}\left\langle\tilde{\psi}_n(\mathbf{q}_1)\tilde{\psi}_n(\mathbf{k}_\perp-\mathbf{q}_2)\right\rangle\left\langle\tilde{\psi}_n(\mathbf{q}_2)\tilde{\psi}_n(\mathbf{k}_\perp-\mathbf{q}_1)\right\rangle \\
&+ \frac{1}{|\Omega|^2}\sum_{\mathbf{q}_1,\mathbf{q}_2}\left\langle\tilde{\psi}_n(\mathbf{q}_1)\tilde{\psi}_n(\mathbf{q}_2)\right\rangle\left\langle\tilde{\psi}_n(\mathbf{k}_\perp-\mathbf{q}_1)\tilde{\psi}_n(\mathbf{k}_\perp-\mathbf{q}_2)\right\rangle \\
&= \delta_{\mathbf{k}_\perp,0} + \frac{2}{|\Omega|}\int\frac{dq_x dq_y}{(2\pi)^2}\,C(\mathbf{q})C(\mathbf{k}_\perp-\mathbf{q})\,.
\end{aligned} \tag{S44}$$

Geometrically, it is the convolution of two Berry's circles. Performing the integral, we obtain

$$\langle|\tilde{I}_n(\mathbf{k}_\perp)|^2\rangle = \delta_{\mathbf{k}_\perp,0} + \frac{1}{|\Omega|}\,\frac{8}{k}\,\frac{\Theta(4E_n-k^2)}{\sqrt{4E_n-k^2}}\,, \tag{S45}$$

where $\Theta(x)$ is the Heaviside step-function. This result implies that the Fourier spectrum of the random variable $\tilde{I}_n(\mathbf{k}_\perp)$ exhibits the following features in the momentum space: a trivial δ-function peak at the origin, an inverse-k divergence at $k=0$, and an inverse square-root divergence at the ring of radius $k=2\sqrt{E_n}$. At these two special k's, the two Berry's circles in the convolution are tangent to one another, which causes the enhancement.

The Fourier spectrum of the GF $G(x,y;x,y)$, which is representative of the s-SNOM signal $S(x,y)$, possesses the same key features. Indeed, neglecting correlations among different eigenfunctions and replacing the summation over n by integration over the density of states $g(E)=\Theta(E)/(4\pi)$ in 2D, we find

$$\langle|\tilde{G}(\mathbf{k}_\perp)|^2\rangle = \frac{1}{|\Omega|^2}\int\frac{g(E)dE}{\left|E-k_0^2\right|^2}\langle|\tilde{I}_n(\mathbf{k}_\perp)|^2\rangle \simeq \frac{1}{|\Omega|^2}\,\frac{2}{Qk_0^2}\,\frac{\Theta(4|k_0|^2-k^2)}{k\sqrt{4|k_0|-k^2}} \tag{S46}$$

for $\mathbf{k}_\perp \neq 0$ and $Q=\frac{1}{2}\operatorname{Re}k_0/\operatorname{Im}k_0 \gg 1$.

In contrast to chaotic systems, billiards of regular geometries, such as a square or an equilateral hexagon, should exhibit highly structured discrete momentum distributions. Therefore, as the boundary complexity increases with successive iterations of the Koch snowflake billiard, we expect to see the emergence of the isotropic rings in the momentum space. Indeed, as illustrated in Fig. S2, the Fourier transform of representative eigenfunction computed for a hexagon billiard exhibits discrete points reflecting its six-fold symmetry. As the billiard geometry becomes more fractal-like, these discrete points transition into a continuous, isotropic ring. The same trend is seen in the s-SNOM data, Fig. 4 of the main text, providing a signature of chaotic phonon-polariton eigenmodes in hBN billiards.

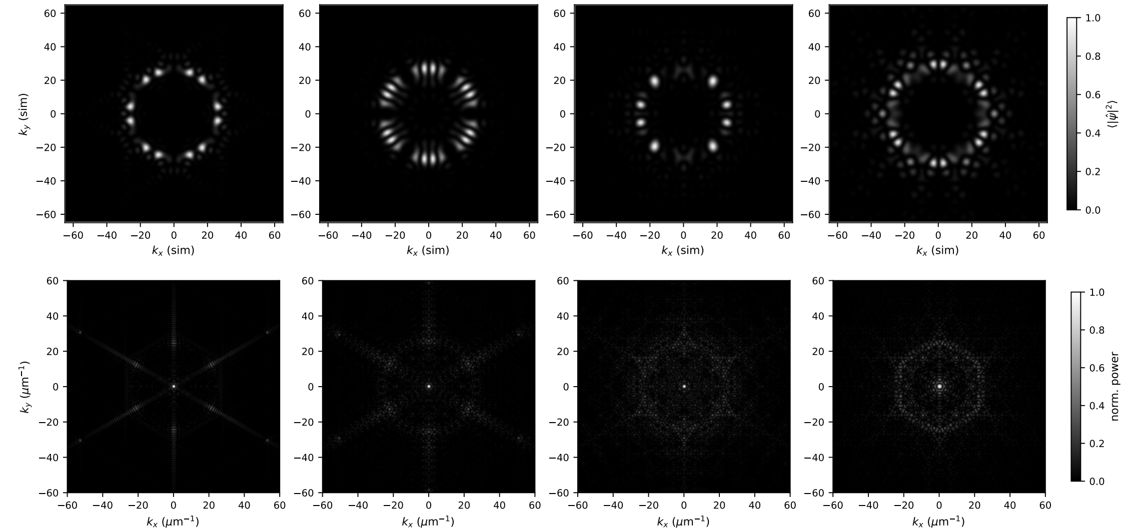

FIG. S2. Top row: Fourier transform of ψ. Bottom Row: Fourier transform of the absolute value $|G|$ of the Green's function, with quality factor $Q = 100$.

G. Level statistics

To characterize the quantum chaotic nature of the phonon polaritons, we analyze the statistical distribution of the cavity's energy levels. In systems where the corresponding classical dynamics is integrable, the level statistics follow Poisson-like spectral statistics. Conversely, in classically chaotic systems, such as the Sinai billiard, the energy levels exhibit level repulsion characterized by Wigner-Dyson statistics [7, 8].

To systematically compare the eigenmodes of our cavities with these universal predictions, we performed the spectral unfolding procedure. We mapped the raw eigenvalues to a dimensionless set of unfolded levels ϵ_n such that the mean level spacing is normalized to unity [9]. This unfolding relies on analyzing the cumulative spectral staircase function,

$$N(E) = \sum_n \Theta(E - E_n),$$

which counts the total number of eigenmodes up to a given number E. We separate the exact empirical staircase $N(E)$ into a smooth, continuous background $\bar{N}(E)$ and a fluctuating component $\delta N(E)$

$$N(E) = \bar{N}(E) + \delta N(E).$$

The leading smooth behavior for a two dimensional billiard of area $|\Omega|$ is governed by Weyl's Law, $\bar{N}(E) = \frac{E}{4\pi}|\Omega|$. (It follows from the property that the density of states $g(E) = \frac{1}{4\pi}$ is constant in

2D.) To account for finite-size boundary corrections, we calculate the residual fluctuations $\delta N(E) = N(E_n) - \bar{N}(E_n)$ and fit them with a polynomial $p(k)$, $k = \sqrt{E}$, of degree 3 to 20 [10]. We have verified that the specific choice of degree within this range does not affect the final unfolding results. The unfolded eigenvalues ϵ_n are then obtained by

$$\epsilon_n = \bar{N}(E_n) + p(\sqrt{E_n}\,).$$

From this normalized spectrum, we evaluate the nearest-neighbor spacings $s_n = \epsilon_{n+1} - \epsilon_n$. The probability density function of these spacings, $P(s)$, serves as a primary diagnostic for wave chaos.

As demonstrated in Fig. 2m,n of the main text, regular integrable geometries (such as the square billiard) yield Poisson distribution, $P(s) = e^{-s}$. In contrast, chaotic geometries (such as the Sinai billiard) exhibit modeled by the GOE Wigner surmise

$$P(s) = \frac{\pi}{2} s \exp\left(-\frac{\pi}{4} s^2\right).$$

3. SUPPLEMENTARY EXPERIMENTAL DISCUSSION

A. Impact of billiard and scatterer sizes

As discussed in the main text, the formation of scarred eigenmodes requires the intrinsic polariton propagation length to exceed the characteristic cavity dimensions. With an approximately constant quality factor, the propagation length is primarily controlled by the polariton wavelength, and therefore by the excitation energy. Figures S3a to f compare devices measured at different excitation frequencies (1465 to 1500 cm^{-1}) and identical hBN thickness, ensuring the same free polariton wavelength within each image. Under these fixed conditions, the billiard size and the relative size of the central obstacle strongly modify the spatial structure of the eigenmodes. The first number in parentheses denotes the ratio of the central perimeter to the cavity width (0.3, 0.4, 0.5), while the second indicates the cavity width (3, 4, 5 μm). Figures S3f to j present the same datasets over a larger field of view with an expanded intensity scale to emphasize enhanced scarring features.

The scarred modes evolve systematically with polariton wavelength, cavity size, and geometric ratio. In general, smaller cavities and larger central obstacle ratios favor stronger scar formation. At shorter wavelengths (Fig. S3a, f), cross shaped scars are most pronounced only for the smallest billiards such as (0.4, 3) and (0.3, 3). As the wavelength increases (Fig. S3b, g), similar patterns emerge in the (0.5, 4) cavities due to its large obstacle ratio. At intermediate wavelengths

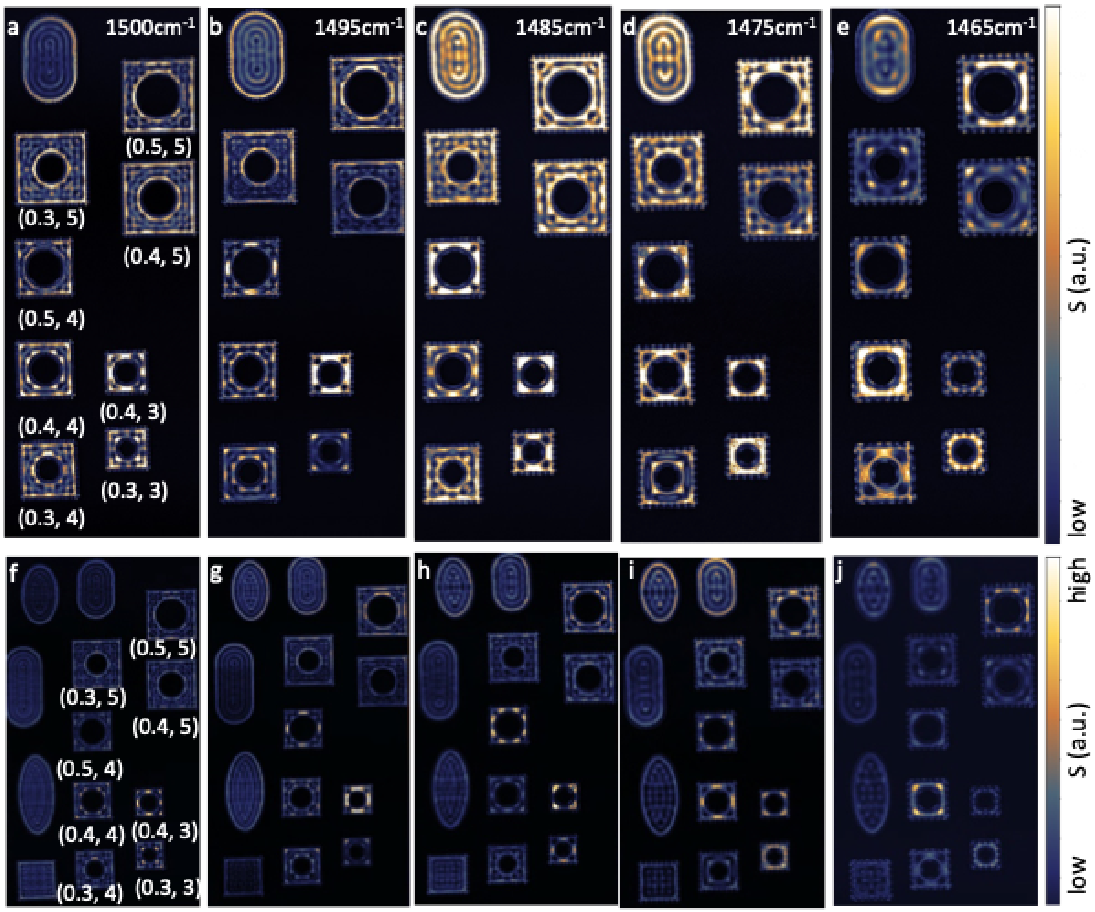

FIG. S3. Geometric dependence of phonon polariton eigenmodes in Sinai billiards. Near field imaging maps are acquired for devices with the same thickness, 54 nm while varying the size, geometric ratio, and excitation energy. The first number in parentheses denotes the ratio of the central perimeter to the billiard width (0.3, 0.4, 0.5), and the second number indicates the cavity width (3, 4, 5 μm). Representative images are shown at six excitation frequencies, (f–j) The same data as (a–e) with zoomed-out area and zoomed-out color scale to illustrate the relative brightness of scars.

(Fig. S3h), cross shaped scars transform into whispering gallery modes in (0.5, 4) cavity and into bright corner localized states in (0.4, 3). With further polariton wavelength increase (Fig. S3d), cross shaped scars dominate in (0.4, 4), while whispering gallery modes develop in both (0.5, 4) and (0.3, 3). The corner bright state for (0.4, 3) also become whispering gallery modes in Fig. S3e. For the largest cavities (5 μm), scarring becomes prominent only at the longest wavelengths 1465 and 1475 cm^{-1}.

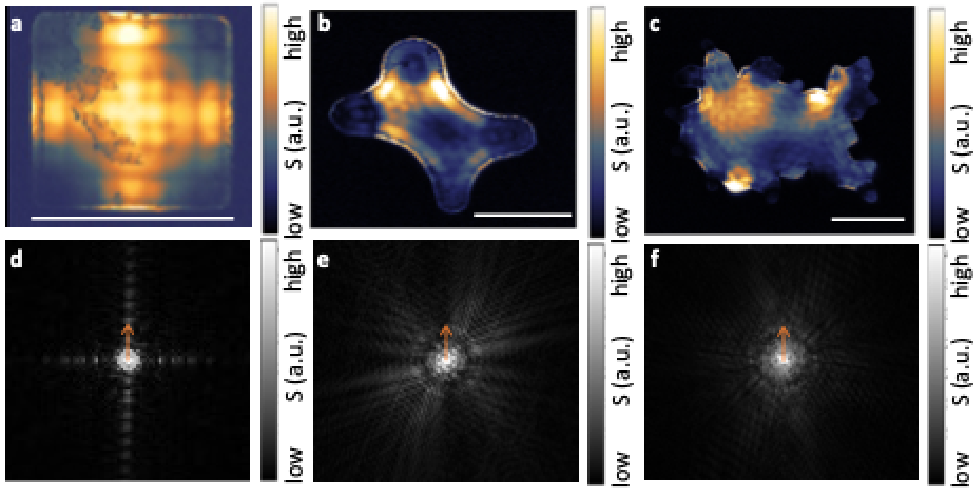

FIG. S4. First row (a-c): SNOM images taken on a. square billiard, b. an asymmetric bone-shape billiard with four convex boundaries of different curvatures. c. a billiard with completely random boundary. Scale bars, 2 μm. Second row: Corresponding FFT maps. The orange arrow point towards the momentum ring corresponding to the dominant $l = 1$ modes in real space images. All data taken on 68 nm-thick $hB^{10}N$ with a 1429 cm^{-1} laser.

B. More billiards for testing Berry's conjecture

As shown in Fig. S4 a and d, similar to the hexagon billiard in the main text, the polariton fields in a square billiard show C_4 symmetry in FFT as an integrable control. For non-integrable shapes, such as a bone with four different curvatures (Fig. S4 b and e)and a random map billiard (Fig. S4 c and f), the polariton momenta can access random directions which manifest themselves as an isotropic ring in FFT. This behavior further confirms the universality of Berry's random wave conjecture, in addition to the high-order Koch billiards studied in the main text.

C. Impact of probe perturbation

In Fig. 2 of the main text, we briefly demonstrated that the probe amplitude can tune the scarred polariton mode patterns in Sinai billiards. This perturbation effect applies to other chaotic billiards as well such as the second and third order Koch billiards. As shown in Fig. S5, comparing the first and third columns, as well as the second and fourth columns, all parameters are kept the same except for probe amplitude. It is evident that the brightened scarring modes around the convex edges are enhanced with a larger probe amplitude. In the corresponding momentum space (second row), larger probe amplitude also leads to a more isotropic Berry's ring with randomized distribution.

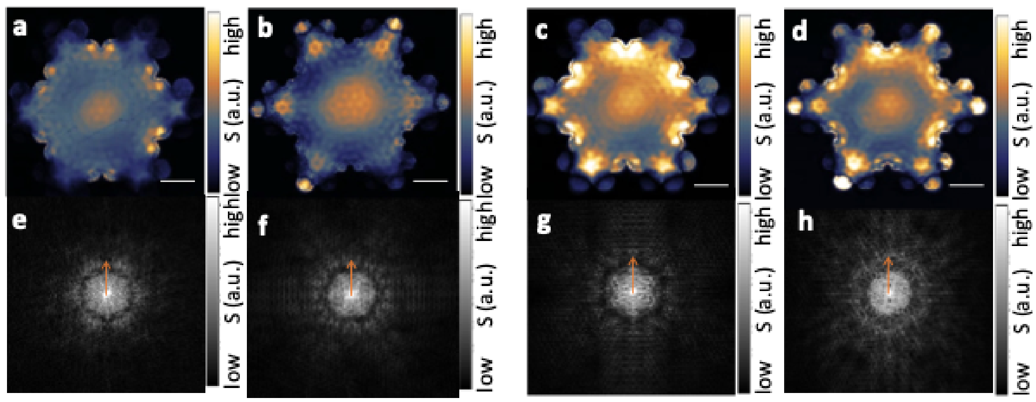

FIG. S5. SNOM images of polaritons in second (a, c) and third (b, d) order Koch snowflakes taken on 68 nm-thick $hB^{10}N$ with 1429 cm^{-1} laser with different probe amplitudes: a–b, 66 nm, c–d, 106 nm. e–f, corresponding FFT maps of a–c. The orange arrows mark the $l = 1$ polariton momenta.

The probe amplitude is a tapping-mode atomic force microscopy (AFM) parameter that corresponds to the average oscillation height of the metallic tip above the sample surface. As shown in Fig. S6d, the probe amplitude is typically on the order of one hundred nanometers, which is one order of magnitude smaller than the near-field polariton wavelength and two orders of magnitude smaller than the far-field excitation wavelength.

To address the tip height effect within 2D Green's function framework, we tentatively consider the role of tip as a dipole with different distances above the 2D sample in Fig. S6. As established above, with weak probe-sample coupling, the s-SNOM signal is primarily governed by the intrinsic electromagnetic response of the sample where the polariton interference patterns are quasi-static responses associated with the sample Green's function. We can further project pre-calculated sample responses onto tip excitation and collection vectors derived from a dipole model, and spatially evaluate the results to emulate a raster-scan measurement. This formulation therefore describes the role of the tip as an effective weighting of intrinsic sample responses, which can lead to different polariton mode patterns, as demonstrated in Fig. S6.

Another related parameter for detecting probe perturbation is the demodulation order, which is detailed in ref [28] of the main text. Higher-order demodulations in s-SNOM experiments provide effectively more information from lower tip heights. This parameter is typically not relevant in capturing the polariton field-profile distribution, i.e., demodulation orders higher than 2 should provide

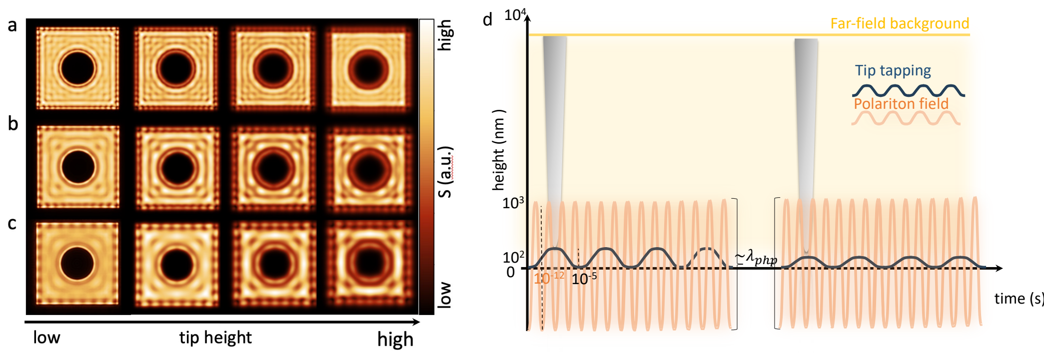

FIG. S6. a–c. Simulated tip height impact on detected mode shapes. d. Illustration of the length scale for probe amplitude, polariton field, and far-field background.

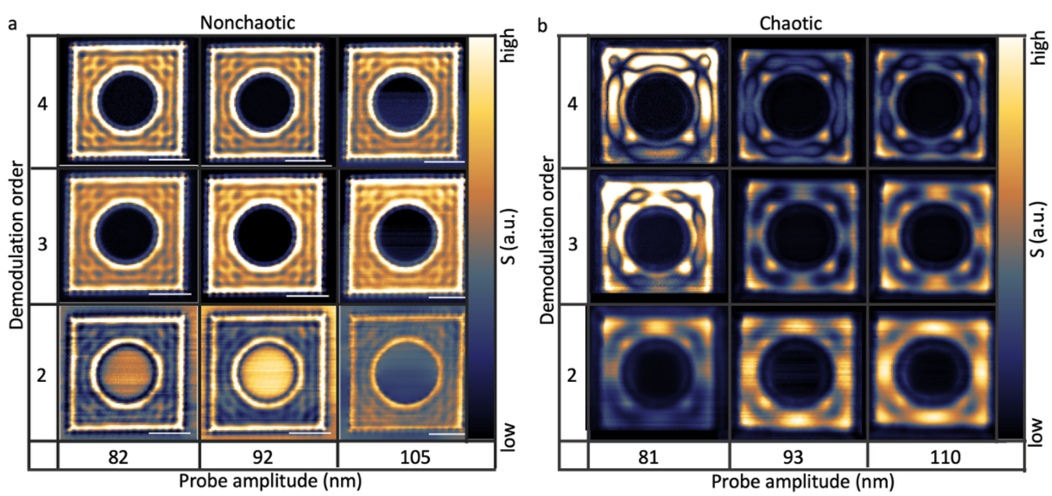

FIG. S7. a. s-SNOM images acquired at $\omega = 1430 cm^{-1}$ on a 10-nm thick billiard. The y-axis denotes different demodulation orders and the x-axis shows the probe amplitude.The propagation lengths and quality factors are low and therefore the chaotic effects have not emerge. The mode shapes remains identicle despite the absolute amplitude differences. b. s-SNOM images acquired at $\omega = 1493 cm^{-1}$ on a 72-nm thick billiard. The propagation lengths and quality factors are high enough to support chaotic effects. Here the mode patterns are visually altered by demodulation order and probe amplitude.

identical field distribution patterns despite different absolute magnitudes of signals. However, as shown in representative data in Fig. S7, the sensitivity from probe amplitudes and demodulation orders are very prominent in the chaotic regime in our single-color imaging experiments, which are not observed in non-chaotic regime.

The mechanism by which probe amplitude and demodulation order modify the detected polariton modes in chaotic billiards can be understood qualitatively as follows. First, during polariton excitation, variations in tip height correspond to different launching conditions, altering the initial near-field profile and consequently the resulting electromagnetic field distribution. Second, during detection, signals collected at different tip heights effectively sample different two-dimensional slices of the three-dimensional polariton mode profile, an effect beyond the scope of our present simulations. Importantly, both the tip-tapping and demodulation frequencies are approximately seven orders of magnitude slower than the characteristic polariton dynamics, such that the measured near-field response represents a time-averaged, steady-state distribution of the polariton billiard modes.

---

[1] S. Dai *et al.*, Tunable phonon polaritons in atomically thin van der Waals crystals of boron nitride, Science **343**, 1125 (2014).

[2] D. A. Svintsov and G. V. Alymov, Refraction laws for two-dimensional plasmons, Phys. Rev. B **108**, L121410 (2023).

[3] B.-Y. Jiang, E. J. Mele, and M. M. Fogler, Theory of plasmon reflection by a 1D junction, Opt. Express **26**, 17209 (2018).

[4] V. A. Volkov and S. A. Mikhailov, Edge magnetoplasmons - low-frequency weakly damped excitations in homogeneous two-dimensional electron systems, Sov. Phys. JETP **67**, 1639 (1988).

[5] J. Schöberl, C++11 implementation of finite elements in NGSolve (2014).

[6] M. V. Berry, Regular and irregular semiclassical wavefunctions, J. Phys. A **10**, 2083 (1977).

[7] M. L. Mehta, *Random Matrices*, 3rd ed. (Academic Press, New York, 2004).

[8] M. V. Berry and M. Tabor, Level clustering in the regular spectrum, Proc. Roy. Soc. London. A **356**, 375 (1977).

[9] H. Yan, Spacing ratios in mixed-type systems, Phys. Rev. E **111**, 054213 (2025).

[10] A. A. Abul-Magd and A. Y. Abul-Magd, Unfolding of the spectrum for chaotic and mixed systems, Physica A **396**, 185 (2014).